# Three-Dimensional Kinematic and Microphysical Evolution of Florida Cumulonimbus. Part I: Spatial Distribution of Updrafts, Downdrafts, and Precipitation

SANDRA E. YUTER AND ROBERT A. HOUZE JR.

*Department of Atmospheric Sciences, University of Washington, Seattle, Washington*

(Manuscript received 31 March 1994, in final form 30 November 1994)

## ABSTRACT

This paper is the first in a three-part study that examines the kinematic and microphysical evolution of Florida cumulonimbus and focuses on the convective-to-stratiform transition of the storm. This first paper lays the groundwork for the subsequent papers by defining the problem under study, delineating the setting for the storm, and describing the spatial distribution of updrafts, downdrafts, and precipitation.

High-resolution radar data of a typical line of storms associated with the Florida sea breeze is the centerpiece of this study. The high-resolution data reveal details of the internal structure of the squall line that were beyond the resolution of previous squall-line studies. Radar reflectivity filled in between cells at upper levels as the storm evolved. Reflectivity values were only weakly associated with updraft and downdraft magnitude. The updrafts and downdrafts in the storm tended to be irregular in their three-dimensional shape and less than 5 km in horizontal extent. At any given time, updrafts and downdrafts at a variety of strengths were present at all levels throughout the storm. The stronger drafts were usually closer to the leading edge of the storm. Upper-level downdrafts were often located alongside upper-level updrafts. Updrafts tended to drift upward from lower levels and weaken as they aged.

## 1. Introduction

This paper is the first in a three-part study [the subsequent papers, Yuter and Houze (1995a,b), are referred to as YH Part II and YH Part III] that examines the kinematic and microphysical evolution of Florida cumulonimbus and focuses on the convective-to-stratiform transition of the storm. This first paper lays the groundwork for the subsequent papers by defining the problem under study, delineating the setting for the storm, and describing the spatial distribution of updrafts, downdrafts, and precipitation. The second and third papers (YH Part II and YH Part III) will build on this information to address the convective-to-stratiform transition of the storm in a more comprehensive, statistical manner.

The Thunderstorm Project (Byers and Braham 1949) showed that thunderstorms usually consist of a fluctuating ensemble of "cells." Each cell consists of an updraft, a precipitation shower, and downdrafts. Low-level downdrafts are driven by melting, evaporation, and hydrometeor drag (Srivastava 1985, 1987; Knupp 1988). Later observations revealed upper-level downdrafts[1] occurring at the sides of the upper portion of updrafts (Heymsfield and Schotz 1985; Smull and Houze 1987; Knupp 1987; Kingsmill and Wakimoto 1991; Raymond et al. 1991; Biggerstaff and Houze 1993; Smull and Augustine 1993).

The Thunderstorm Project showed that as a cell ages its lower portion is taken over by a weak downdraft. Early radar measurements indicated that the character of the precipitation changes as the cell ages (Battan 1973). During its early, highly convective stage, the radar echo is a vertically oriented maximum of reflectivity,[2] while in its later stratiform stage, when the vertical air motions are weaker, the radar echo may exhibit a horizontal bright band (Battan 1973, 190–195; Houze 1993, chapter 6) at the melting level.

Thunderstorms often conglomerate to form "mesoscale convective systems." The precipitation pattern of a mesoscale convective system typically contains both active convective cells and stratiform precipitation, much of which is composed of the remnants of older

---

[1] Downdrafts occurring at middle and upper levels will be referred to as upper-level downdrafts in order to distinguish them from lower-level downdrafts associated with precipitation.

[2] For simplicity, we will use the terms radar reflectivity, reflectivity, or dBZ to refer to the equivalent radar reflectivity factor $Z_e$ in decibel (dB) units with respect to 1 $mm^6$ $m^{-3}$.

---

*Corresponding author address:* Sandra E. Yuter, Department of Atmospheric Sciences, University of Washington, Box 351640, Seattle, WA 98195.

cells (Leary and Houze 1979; Leary 1984; Houze 1989; Houze et al. 1990; Mapes and Houze 1992, 1993). The gross vertical air motion and radar reflectivity characteristics of convective and stratiform regions have been derived from Doppler radar data in field projects such as PRE-STORM[3] (Biggerstaff and Houze 1991a, 1993) and EMEX[4] (Mapes and Houze 1993) and from single-Doppler and composite sounding analyses in other locations around the world (Houze 1989).

A primary limitation of previous studies mentioned above is that the horizontal spatial resolution of the radar data collected has been insufficient to reveal the processes whereby a group of convective cells in a cumulonimbus complex evolves from a highly convective state to a more quiescent stratiform state. When ground-based dual-Doppler radar data are obtained, a primary factor in determining the spatial resolution of the data is the distance (baseline) separating the two radars (Davies-Jones 1979). In PRE-STORM, the baseline was approximately 60 km. This baseline maximized areal coverage but resulted in coarse spatial resolution. In this study, we examine Doppler radar data obtained during the Convection and Precipitation/ Electrification Experiment (CaPE). This project was conducted in Florida during the summer of 1991. The sea-breeze-triggered convection was similar to that observed in the Thunderstorm Project. In CaPE, a 23-km dual-Doppler baseline was used. In contrast to PRE-STORM, this short baseline maximized spatial resolution at the expense of areal coverage. This study capitalizes on the high spatial resolution provided by this short baseline to study the process of evolution of cells from convective toward stratiform structure.

## 2. Convective versus stratiform

Since the goal of this study is to elucidate the processes whereby a convective storm takes on a more stratiform structure in its later stages, it is essential to clarify the terms convective and stratiform. It is particularly important to clarify the term stratiform since it is not defined in the Glossary of Meteorology (Huschke 1959) and several definitions of stratiform have been used by different authors (e.g., Houghton 1968; Houze 1973; Leary 1984; Churchill and Houze 1984; Houze et al. 1990). Some definitions are based on vertical radar reflectivity structure, such as the presence of a radar bright band. Other definitions include an area of weaker and/or more uniform reflectivity values either adjacent or subsequent to a convective region, and an

area of weaker vertical velocities compared to those in the convective region.

Most of the working definitions alluded to above refer to the structure or pattern of precipitation. The underlying reason for the different appearance of convective and stratiform precipitation, however, lies in the different nature of the vertical air motions producing them (Houghton 1968; Houze 1981, 1993, chapter 6). The distinction of precipitation process based on vertical air motion is the definition of convective versus stratiform used here. Stratiform conditions are present when

$$|w| \ll |V_{ice}|, \tag{1}$$

where $w$ is the vertical air velocity, and $V_{ice}$ is the terminal fall speed of precipitation-sized ice crystals and snow particles ($\sim 1-3$ m s$^{-1}$). When this condition does not hold, that is, when

$$|w| \geq |V_{ice}|, \tag{2}$$

conditions are defined as convective. The terms transition or intermediary have been used by some authors (Biggerstaff and Houze 1991a, 1993; Mapes and Houze 1993; Braun and Houze 1994) to describe areas of mesoscale convective systems where vertical velocities are weakening toward the point where Eq. (1) holds.

This stratiform definition, based on weak vertical air motion, such that the precipitation-sized ice particles fall relative to the ground, implies an associated reflectivity structure. At upper and middle levels, the heavier precipitation particles with their higher fall speeds are not found. The lighter ice particles at these upper levels fall slowly. The precipitation-sized ice particles grow in size when they are falling within regions of weak atmospheric ascent. These slowly falling ice particles aggregate above the 0°C level to form highly reflective large particles. They melt within a narrow layer, where a radar bright band is produced. Thus, the associated reflectivity structure of precipitation-sized ice particles within stratiform precipitation exhibits nearly uniform reflectivity at each level and increasing reflectivity with decreasing height. The maximum value of reflectivity within stratiform precipitation is attained at the bright band. Since the vertical velocity structure causes the associated reflectivity structure, a definition of stratiform conditions in terms of vertical velocity (as first suggested by Houghton 1968) is more fundamental than definitions based solely on the pattern of precipitation.

## 3. Observational setting

### a. Data sources

CaPE was conducted in east-central Florida from 8 July to 18 August 1991 (Figs. 1a,b). The sensors used for this study include the National Center for Atmo-

spheric Research (NCAR) CP-2, CP-3, and CP-4 radars (Table 1), the NCAR Portable Automated Mesonet (PAM) (Brock and Govind 1977; Brock and Saum 1983), NCAR Cross-chain Loran Atmospheric Sounding System (CLASS) (Lauritsen et al. 1987), and the South Dakota School of Mines and Technology (SDSMT) T-28 research aircraft (Johnson and Smith 1980; Detweiler and Smith 1992). The CP-3 and CP-4 C-band (5-cm wavelength) radars scanned in coordinated dual-Doppler mode. The shaded areas in Fig. 1b

TABLE 1. Selected characteristics of NCAR radars during CaPE.

| | CP-2 | | CP-3 | CP-4 |
| | S-band | X-band | C-band | C-band |
|---|---|---|---|---|
| Wavelength (cm) | 10.7 | 3.2 | 5.5 | 5.5 |
| Average transmitted power (dBm) | 59 | 43 | 58.5 | 59.1 |
| Beamwidth (deg) | 0.91 | 0.95 | 0.9 | 0.9 |

are the dual-Doppler lobes: the areas where the wind field can be calculated from the radial velocity data of the intersecting radar beams. The S-band (10-cm wavelength) portion of the CP-2 radar provided reflectivity and differential reflectivity data, and the SDSMT T-28 supplied flight-level data from cloud penetrations.

On the afternoon of 15 August 1991, a line of convection near Melbourne, Florida, was initiated by the interaction of the sea breeze and an eastward-moving outflow from a thunderstorm farther inland. The southern end of the line of thunderstorms was in the southern dual-Doppler lobe of the C-band radars (Fig. 1b), which afforded the opportunity for radar coverage of the development of the storm from initiation, through mature convection, and toward a stratiform state. The SDSMT T-28 flew through the line of thunderstorms during its early stages of development. In addition, CP-2 scanned the region during the initial period of storm development.

### b. Synoptic situation

The 1200 UTC[5] synoptic-scale surface pressure and 500-hPa maps (Fig. 2) for 15 August 1991 reveal no synoptic-scale disturbances affecting the region of the Florida peninsula. The sea level pressure field (Fig. 2a) shows that no fronts were present in the eastern United States. A weak surface heat low was centered in northeastern Mexico, and the seasonal subtropical high over the Atlantic Ocean was present. The low-level winds (Fig. 2a) were west-southwesterly over most of the peninsula, which is characteristic of development of afternoon storms on the east coast of the peninsula (Gentry and Moore 1954; Blanchard and Lopez 1985). Winds backed to southerly with height (Fig. 2b).

Soundings taken at Deer Park, in the center of the south lobe of dual-Doppler radar observations (Fig. 1b), are shown in Fig. 3. The afternoon 1956 UTC sounding (Fig. 3b) taken just prior to storm development exhibited stronger winds aloft and slightly moister air below 700 hPa, with an associated increase in convective available potential energy [CAPE; Houze (1993) p. 283] compared to the morning 1653
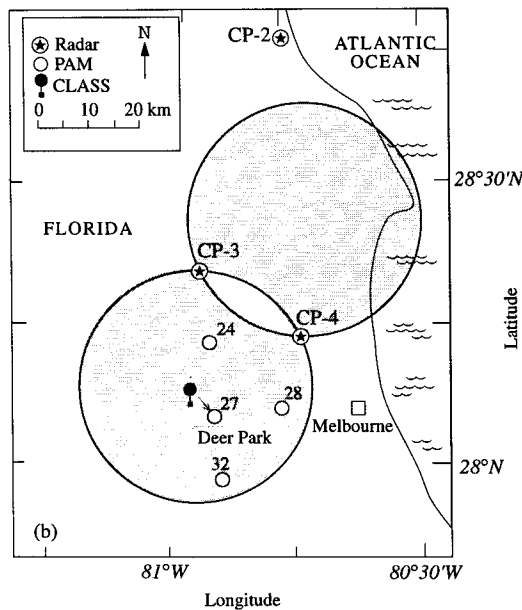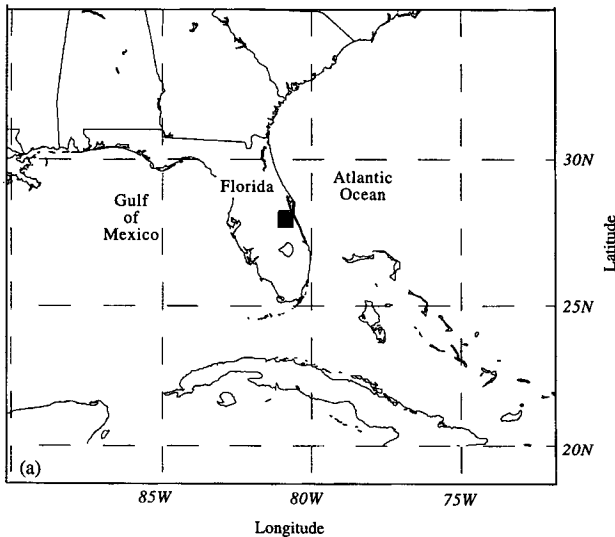


FIG. 1. (a) Map of southeastern United States centered on Florida; square indicates location of radar analysis within the CaPE domain. (b) Map of CaPE domain showing location of field observation instruments used in this study. The CP-3/CP-4 dual-Doppler lobes are shaded. PAM mesonet stations are identified by number (24, 27, 28, 32).

---

[5] Times given in this study will be in universal time coordinated (UTC). Local standard time is UTC − 4 h.
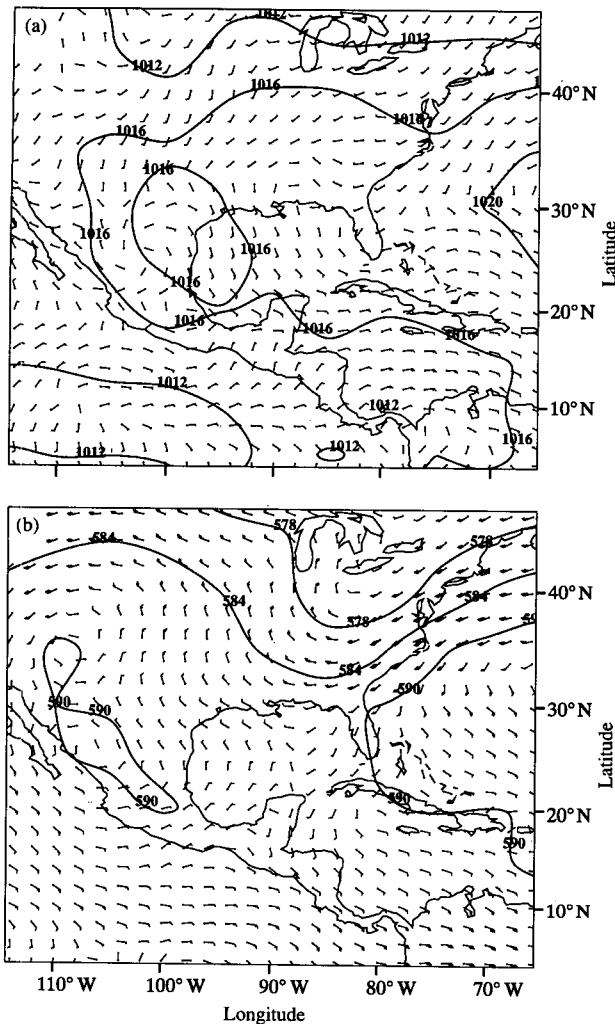
FIG. 2. The 1200 UTC 15 August 1991 aviation model initialization synoptic maps centered in the Gulf of Mexico. (a) Surface pressure (hPa) and 1000-hPa wind vectors. (b) 500-hPa heights (dam) and wind vectors. Full wind barb is 5.m s$^{-1}$.

UTC sounding (Fig. 3a). The 1956 UTC sounding was characterized by weak vertical wind shear. Low-level southeasterly winds indicate the ocean side of the low-level sea-breeze convergence. The 1956 UTC Deer Park sounding has CAPE = 614 J kg$^{-1}$, lifted index[6] LI = $-2.4$, and bulk Richardson number (Ri) = 73.7 corresponding to the range (Ri > 40) that Weisman and Klemp (1982) found to favor multicellular convective structure. The 0°C level was at 4.4 km MSL and the equivalent potential temperature $\theta_e$ minimum was 325 K at 4.5 km. The prestorm environment shown by these soundings is similar to that used in two-dimensional sea-breeze convection model runs of Nich-

---

[6] Galway (1956).

olls et al. (1991), except that the 15 August 1991 sounding was slightly warmer at the surface and slightly dryer at midlevels. The sounding taken at 2219 UTC (Fig. 3c) within the dissipating storm had a temperature inversion just above the surface, consistent with a cold pool at the surface.

### c. Sea-breeze convection

The multicellular thunderstorm that occurred on 15 August 1991 in the southern dual-Doppler lobe was typical of deep convection during the sea-breeze regime in the Florida summer. According to Burpee and Lahiff's (1984) classification scheme derived from a climatological study of Florida storms, days with less than 30% high cloudiness at sunrise are classified as sea-breeze days. These days exhibit strong diurnal variation of rainfall, with 91% occurring during the afternoon to early evening (1400–0200 UTC). The clear skies over the Florida peninsula at 1300 UTC (Fig. 4a) thus classify 15 August 1991 as a sea-breeze day. Also consistent with this classification, thunderstorm activity in the CaPE area on 15 August 1991 peaked in the afternoon at roughly 2200 UTC (Fig. 4f) and was dissipating by evening (2300 UTC 15 August 1991–0100 UTC 16 August 1991; Figs. 4g–i).

### d. Satellite overview

The GOES infrared (IR) imagery shown in Fig. 4 reveals the development of the storm under study in relation to other convective activity over the Florida peninsula. Cloud-top temperatures between 235 and 208 K and less than 208 K are highlighted in the figure. The satellite data show that convection developed on the west and south coasts of the peninsula (Figs. 4b,c) and that the storm on the west coast moved eastward with the low-level wind, interacting with the east coast sea breeze to trigger additional convection in the late afternoon (2000–2100 UTC, Figs. 4d,e). The cirrus cloud shield produced by storms on the southern tip of Florida was advected northward by the prevailing southerly upper-level wind. According to the area of lowest IR temperatures (Fig. 4f), the area under study contained one of the more intense storms of the day, which was related to earlier intense storms centered to the north (Fig. 4e).

### e. Radar echo pattern

Radar reflectivity data from the 3° elevation angle surveillance scans of the CP-4 radar illustrates the evolution of the rainfall pattern associated with the storm (Fig. 5). This study focuses on the area in the southern dual-Doppler lobe indicated by the box in Fig. 5 during the period between 2120 and 2240 UTC. Convection was active north of the dual-Doppler lobes at 2000 (not shown). Storm activity had moved south into the CaPE domain by 2030 (Fig. 5a). By 2100 UTC (Fig. 5b), a
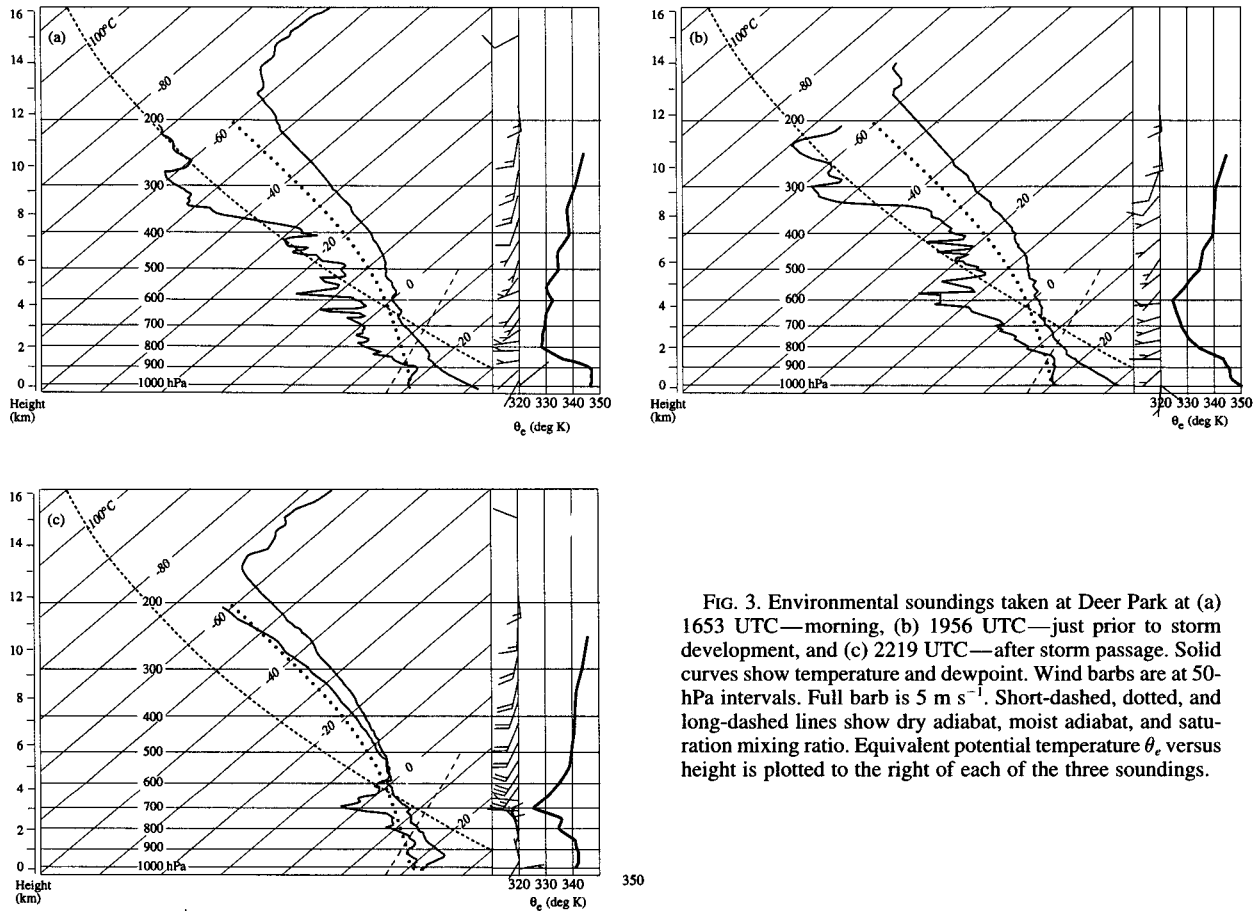
FIG. 3. Environmental soundings taken at Deer Park at (a) 1653 UTC—morning, (b) 1956 UTC—just prior to storm development, and (c) 2219 UTC—after storm passage. Solid curves show temperature and dewpoint. Wind barbs are at 50-hPa intervals. Full barb is 5 m s$^{-1}$. Short-dashed, dotted, and long-dashed lines show dry adiabat, moist adiabat, and saturation mixing ratio. Equivalent potential temperature $\theta_e$ versus height is plotted to the right of each of the three soundings.

line of strong cells had developed on the western edge of the northern dual-Doppler lobe. Isolated cells developing in the southern dual-Doppler lobe behind an eastward-moving surface outflow were augmented by the collision of the outflow and sea-breeze convergence lines at 2117 (not shown). Generally, newer cells formed on the eastern (leading) edge and southern end of the convective line, while the western (trailing) side was occupied by older weakening convective cells. By 2123, some cells had reached heights greater than 10 km. At 2130 (Fig. 5c), a line of cells had developed in the center of the southern dual-Doppler lobe. The squall line broadened, lengthened, and weakened as it matured and moved eastward (2200 UTC, Fig. 5d). By 2230 (Fig. 5e), the main storm activity had moved out of the southern dual-Doppler lobe, with new growth on the southern end of the line outside the lobe. Only the rear portion of the line remained within the dual-Doppler box. At 2300 (Fig. 5f), the last remnants of the squall line still in the southern dual-Doppler lobe were weak and dissipating.

*f. Rainfall*

Rain-rate and total rain accumulation data on 15 August 1991 are shown in Fig. 6 from PAM stations 24,

27, 28, and 32 in the southern dual-Doppler lobe (locations in Fig. 1b). Sampling by rain gauges is very sensitive to the position of individual storm cells relative to the gauge. The spikiness of the plot is partly an artifact of the tipping-bucket measuring method. These plots show brief periods of rain rates greater than 100 mm h$^{-1}$ at two stations. The movement of convective activity eastward is also evident from the gauge traces. PAM stations 27 and 32 began to record heavy showers at about 2123 UTC. PAM station 28, to the east, does not record rain until 2153. The pattern shows individual heavy showers lasting approximately 30 min with rates greater than 20 mm h$^{-1}$ shifting to a period of lighter rain (<20 mm h$^{-1}$) lasting for about 50 min. These records are consistent with the passage of the squall line, with newer cells on its leading side, and weakening cells on its trailing side. The four gauges averaged an accumulation of 23 mm over the period 2120–2300 UTC.

## 4. Data-processing methods

Eight volumes of radar data from the time period 2123–2237 UTC are used to characterize the storm (Table 2). Between 2205 and 2235 equipment prob-
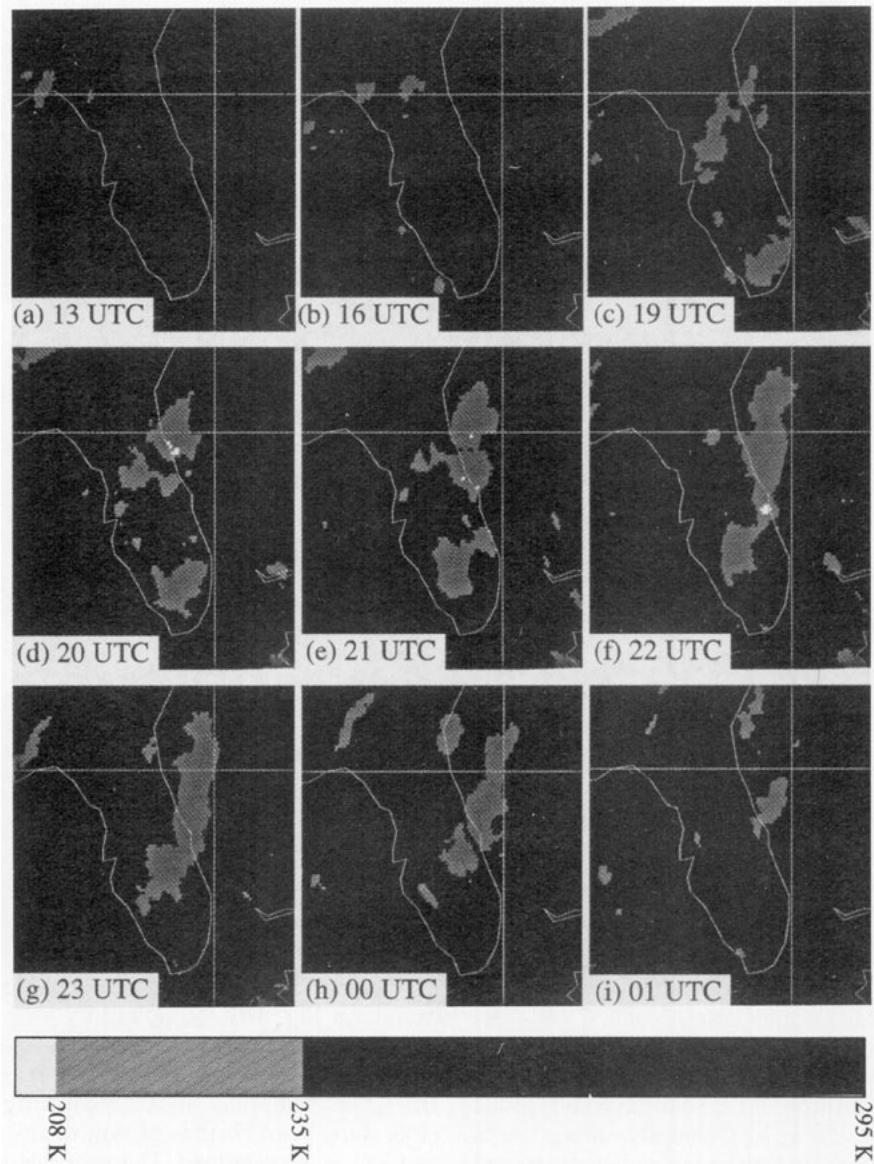
FIG. 4. Time series of GOES IR imagery of the Florida peninsula resampled to 8 km × 8 km resolution from 1300 UTC 15 August to 0100 UTC 16 August 1991. The cloud-top temperatures colder than 208 K, between 208 and 235 K, and warmer than 235 K are color coded: white, gray, and black, respectively.

lems prevented the collection of dual-Doppler data. Five of the radar volumes[7] contain dual-Doppler data from the C-band radars (CP-3 and CP-4). The three remaining volumes contain differential reflectivity $Z_{DR}$

data from CP-2. The processing and analysis of the CP-2 differential reflectivity data are discussed in YH Part II.

Dual-Doppler analysis was performed on the C-band radar volumes by adapting the procedures of Bigger-staff and Houze (1991a) to this dataset. The NCAR RDSS (Oye and Carbone 1981) software was used to unfold (Rinehart 1991, p. 81) radial velocities and to edit the radar reflectivity and radial velocity data to remove apparently spurious data such as second-trip echoes (Rinehart 1991, p. 83) and flare echoes (Wilson

[7] A single time used in association with a radar data volume corresponds to the beginning of the volume scan. For consistency, the volumes of differential reflectivity data from CP-2 are referred to according to the corresponding C-band radar data volume start times. Exact volume times for the CP-2 volumes are given in Table 2.
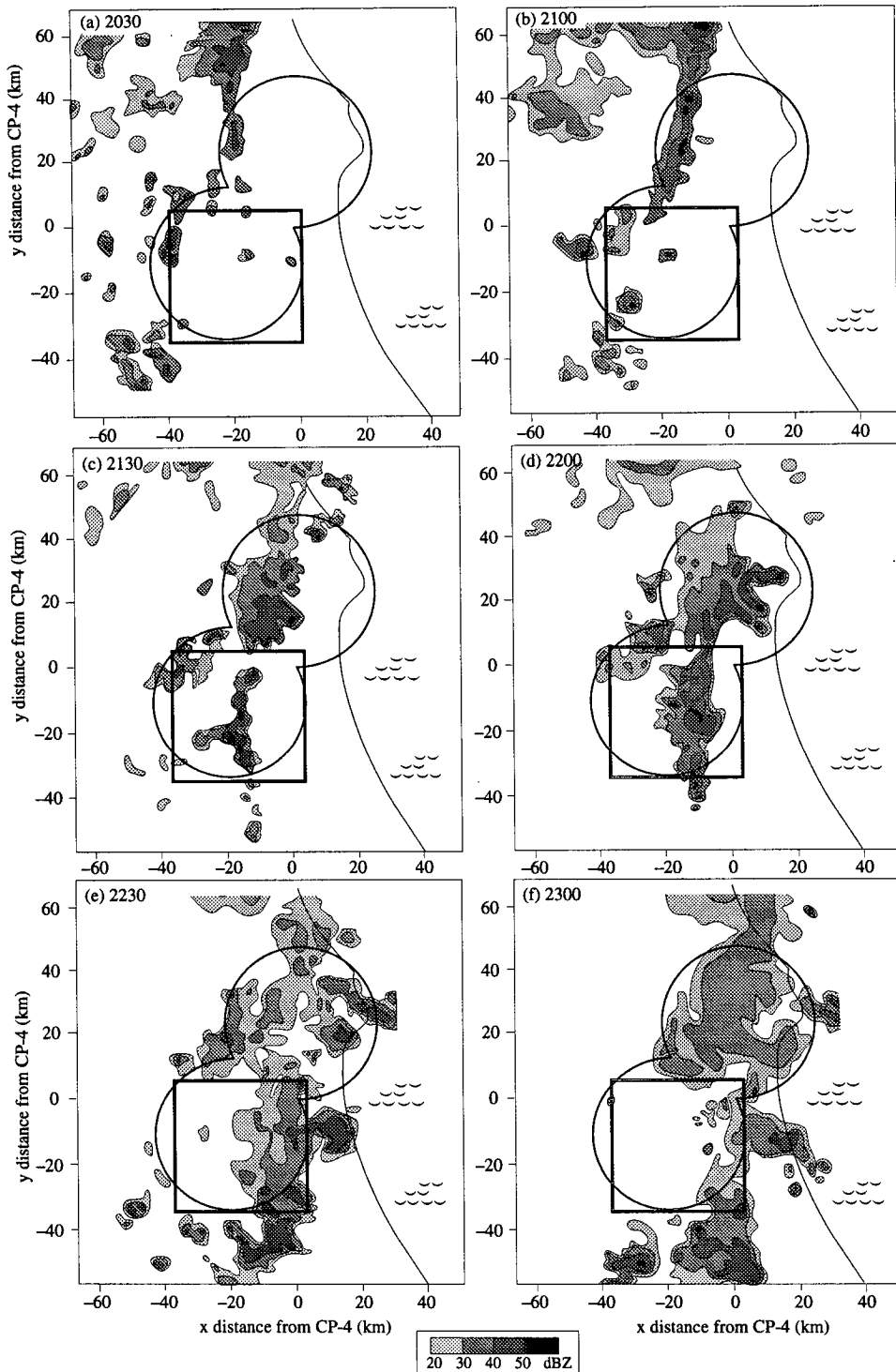
FIG. 5. Time series of 3° elevation surveillance scans of radar reflectivity from CP-4. Dual-Doppler lobes (circles) and area of radar data analysis (box) are indicated. Radar reflectivity is shaded in 10-dB-wide intervals starting at 20 dBZ.

and Reum 1988). NCAR SPRINT (Mohr and Vaughn 1979) was used to interpolate the two fields to a Cartesian grid covering 40 km × 39 km in the horizontal

with 0.5-km spacing and 0–17.2 km MSL in the vertical with 0.4-km spacing. The limited size of the dual-Doppler lobe (Fig. 1b) made it necessary to hold the
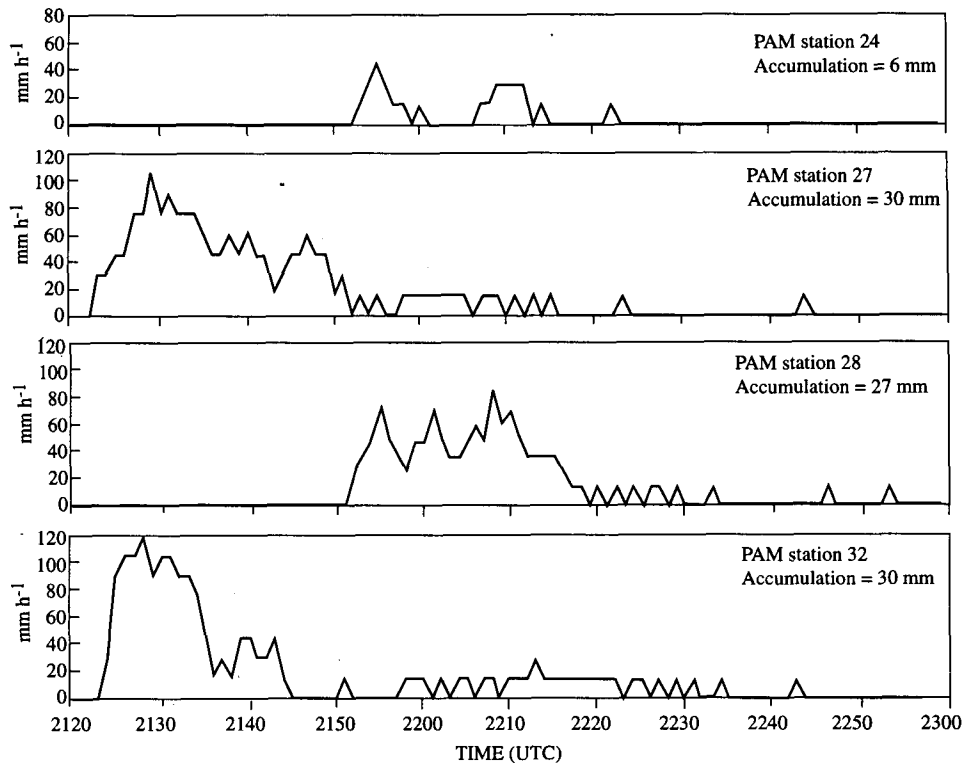
FIG. 6. Rain rates (mm h⁻¹) for four PAM stations (24, 27, 28, 32) within the radar data analysis area (Fig. 1b). Accumulated rainfall at each station between 2120 and 2300 UTC is also shown.

grid stationary, in reference to the earth, for all the volumes, even though the line of storms moved through the grid. Later volumes, especially at 2237 UTC, therefore contained only the trailing portion of the line of storms. However, the movement of the line of storms through the grid did not prevent the documentation of a sequence of life cycle stages of a section of the line of storms.

The radar reflectivity field was determined by taking the maximum of the two C-band radar reflectivities at each grid point. The minimum detectable reflectivity at 50 km was $-18$ dBZ for CP-3 and $-15$ dBZ for CP-4

(Wilson et al. 1994). Fall speeds of particles were computed from reflectivity values with the empirical relationships for rain and snow used by Marks and Houze (1987). A mixed ice–rain layer was used between 4.8 and 5.2 km. The height of the melting layer in a convective storm is difficult to pinpoint. We used a combination of the environmental sounding and close range differential reflectivity data to estimate the melting-level altitude. The vertical resolution of the CP-2 data over the grid volume was insufficient to use the differential reflectivity data in the fall-speed calculation (Steiner 1991). Expected errors in fall velocity are

TABLE 2. Radar data volumes analyzed from 15 August 1991.

| Volume label | Time period (UTC) | Radars | Description |
|---|---|---|---|
| 2123 $Z$ and $w$ | 2123:30–2126:41 | CP-3, CP-4 | Early |
| 2123 $Z_{DR}$ | 2122:56–2125:56 | CP-2 | |
| 2139 $Z$ and $w$ | 2139:31–2142:47 | CP-3, CP-4 | Highly energetic |
| 2139 $Z_{DR}$ | 2138:21–2141:03 | CP-2 | |
| 2144 $Z$ and $w$ | 2144:54–2148:13 | CP-3, CP-4 | Most vigorous |
| 2144 $Z_{DR}$ | 2144:47–2147:54 | CP-2 | |
| 2155 $Z$ and $w$ | 2155:45–2159:32 | CP-3, CP-4 | Mature |
| 2237 $Z$ and $w$ | 2237:44–2242:14 | CP-3, CP-4 | Fading |

highest within rain regions where the radar beam is nearly horizontal and thus will have little effect on this analysis.

The Doppler scans used in this analysis were optimized for high-resolution calculation of the three-dimensional wind field (Burghart et al. 1989) and coordinated such that the implied stationarity of the wind field (time for beams from the two radars to intersect at each grid point) was less than 30 seconds. On average, CP-3 scanned 35 elevation angles and CP-4 scanned 30 elevation angles during each 3–4.5 min of simultaneous[8] Doppler volume collection.

Synthesis of radial velocities into horizontal winds was performed using NCAR CEDRIC (Mohr and Miller 1983). A two-step Leise filter (Leise 1981) was applied to the velocity data to remove horizontal wavelengths less than 2 km. Vertical velocities were calculated by vertical integration of the horizontal divergence field using variational adjustment of the anelastic mass continuity equation to both upper- and lower-boundary conditions (O'Brien 1970; Ray et al. 1980; Ray and Sangren 1983; Kessinger et al. 1987; Matejka and Srivastava 1991; T. Matejka 1994, personal communication). The lower boundary condition was set to zero at the earth's surface. The upper boundary condition was conditional on the upper-level reflectivity field. An upper boundary condition value ($w$ at echo top) of 0.25 m s$^{-1}$ was used where reflectivity within the column above 14 km was greater than 10 dBZ; otherwise, the upper boundary condition was set to zero.

The horizontal velocity error variance associated with the scan geometry and radar baseline is smallest at the center of the dual-Doppler lobe (where between beam angle is 90°) and increases toward the edges of the lobe (where between beam angle is 30°) (Davies-Jones 1979). Although a number of authors (Davies-Jones 1979; Wilson et al. 1984; Kessinger et al. 1988) have methods to calculate velocity error variances, the resulting values are highly dependent on the input values of the variance of radial velocity—a quantity that is in itself difficult to measure accurately. The combination of a 23-km baseline between the sensitive NCAR C-band radars, close scan coordination, and computer optimization of elevation angle sequences make the CaPE data extremely well suited for high-resolution dual-Doppler processing. It follows that application of established dual-Doppler processing techniques to this data will result in a wind analysis with an accuracy comparable to or better than previously published dual-Doppler analyses.

Since the vertical velocity field cannot be measured directly, absolute errors in vertical velocity cannot be

calculated. The appendices of Biggerstaff and Houze (1991a) and Kingsmill and Wakimoto (1991) discuss general sources of error associated with calculation of vertical velocity from dual-Doppler data using methodologies similar to the one used here. To assess the sensitivity of the vertical velocity solution, a variety of upper boundary conditions were tested. While different upper boundary conditions produced slightly different values of $w$ at individual grid points, the pattern of the vertical velocity field and its statistics remained essentially the same. Thus, errors within the horizontal and vertical wind fields will not affect the major conclusions made in this three-part study.

## 5. Cross sections of a multicellular storm

At low spatial resolution, lines of storms associated with the Florida sea breeze have a tendency to appear two-dimensional (Nicholls et al. 1991). The overall pattern for the 15 August 1991 storm was of a roughly north–south line with new growth predominantly on the east and south edges of the line. However, horizontal and vertical cross sections of high spatial resolution radar data obtained during the passage of the storm (e.g., Figs. 7, 8, and 9) reveal a three-dimensional multicellular radar reflectivity pattern that contained a rapidly evolving, complex jumble of updrafts and downdrafts. This three-dimensional structure cannot be reduced to a two-dimensional cross section, such as a spatial composite (Biggerstaff and Houze 1991a,b, 1993), without losing the very detail that has been gained by the high resolution of the measurements.

The high-resolution data of a Florida squall line presents an opportunity to extend previous squall-line studies. Previous studies were limited by coarser resolution data and thus concentrated on the mean and two-dimensional (line-normal) aspects of storm evolution (Smull and Houze 1987; Biggerstaff and Houze 1991a,b, 1993). The three-dimensional evolution of the intensities, spatial distributions, and interrelationships of reflectivity cells, updrafts, and downdrafts in the squall line is revealed in the high-resolution data of this study. This information is important to understanding how convective structures evolve to stratiform structures. This first part of the study begins the process of extracting this information from the high-resolution data with a traditional case study analysis based on cross sections.

### a. Spatial variability

To illustrate some of the features of the spatial variability of the updrafts and downdrafts, four vertical cross sections, all 20 km in length, are taken of the 2139 UTC volume (Fig. 7). The two vertical cross sections, one north–south (A–A' in Fig. 7b) and one southwest–northeast (B1–B1' in Fig. 7c), are centered on the same updraft located at horizontal coordinates $x$

---

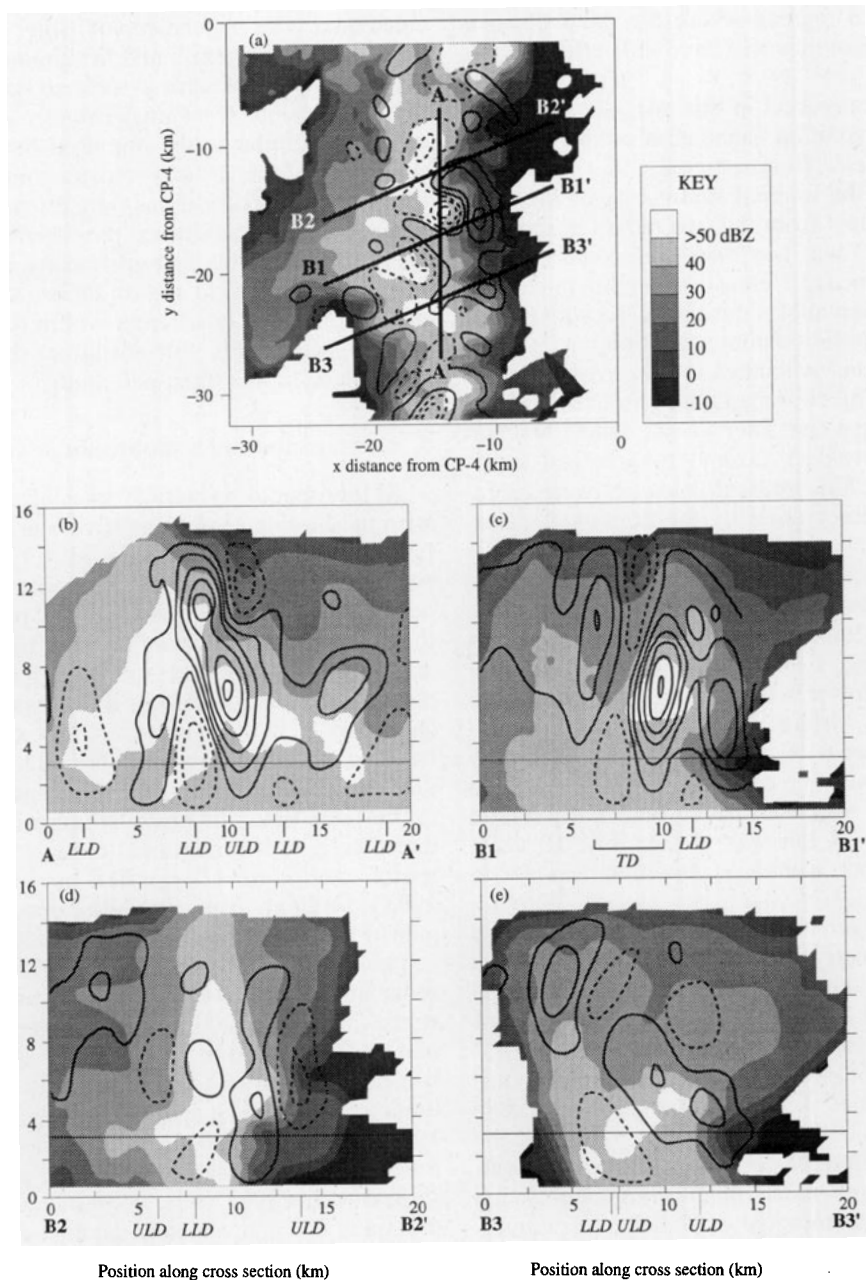[8] The start times of the dual-Doppler scanning sequences were coordinated via radio.

FIG. 7. Horizontal and vertical cross sections of radar reflectivity and vertical velocity through the analyzed 2139 dual-Doppler volume. Reflectivity is shaded at 10-dB intervals starting at −10 dBZ. Horizontal locations of individual upper-level downdrafts (ULD), lower-level downdrafts (LLD), and transverse downdrafts (TD) are indicated along the bottom of each vertical cross section. Height of horizontal cross section in (a) is indicated in the vertical cross sections by the horizontal line at 3.2 km. (a) The 3.2-km altitude horizontal cross section. Four heavy lines, A–A', B1–B1', B2–B2', and B3–B3', indicate vertical cross sections that are 20 km long. Contours are of vertical velocity at −15, −9, −3, 3, 9, and 15 m s⁻¹, with negative values dashed. Cross sections A–A' and B1–B1' are centered on the same updraft located at $x = -14.5$ km, $y = -17$ km. (b) North–south cross section indicated by A–A'; contours of vertical velocity at −9, −3, 3, 9, 15, 21, 27, and 33 m s⁻¹, with negative values dashed. (c) Southwest–northeast cross section indicated by B1–B1'; contours of vertical velocity at −9, −3, 3, 9, 15, 21, 27, and 33 m s⁻¹ with negative values dashed. (d) Southwest–northeast cross section indicated by B2–B2'; contours of vertical velocity at −9, −3, 3, and 9 m s⁻¹, with negative values dashed. (e) Southwest–northeast cross section indicated by B3–B3'; contours of vertical velocity at −3, 3, and 9 m s⁻¹, with negative values dashed.
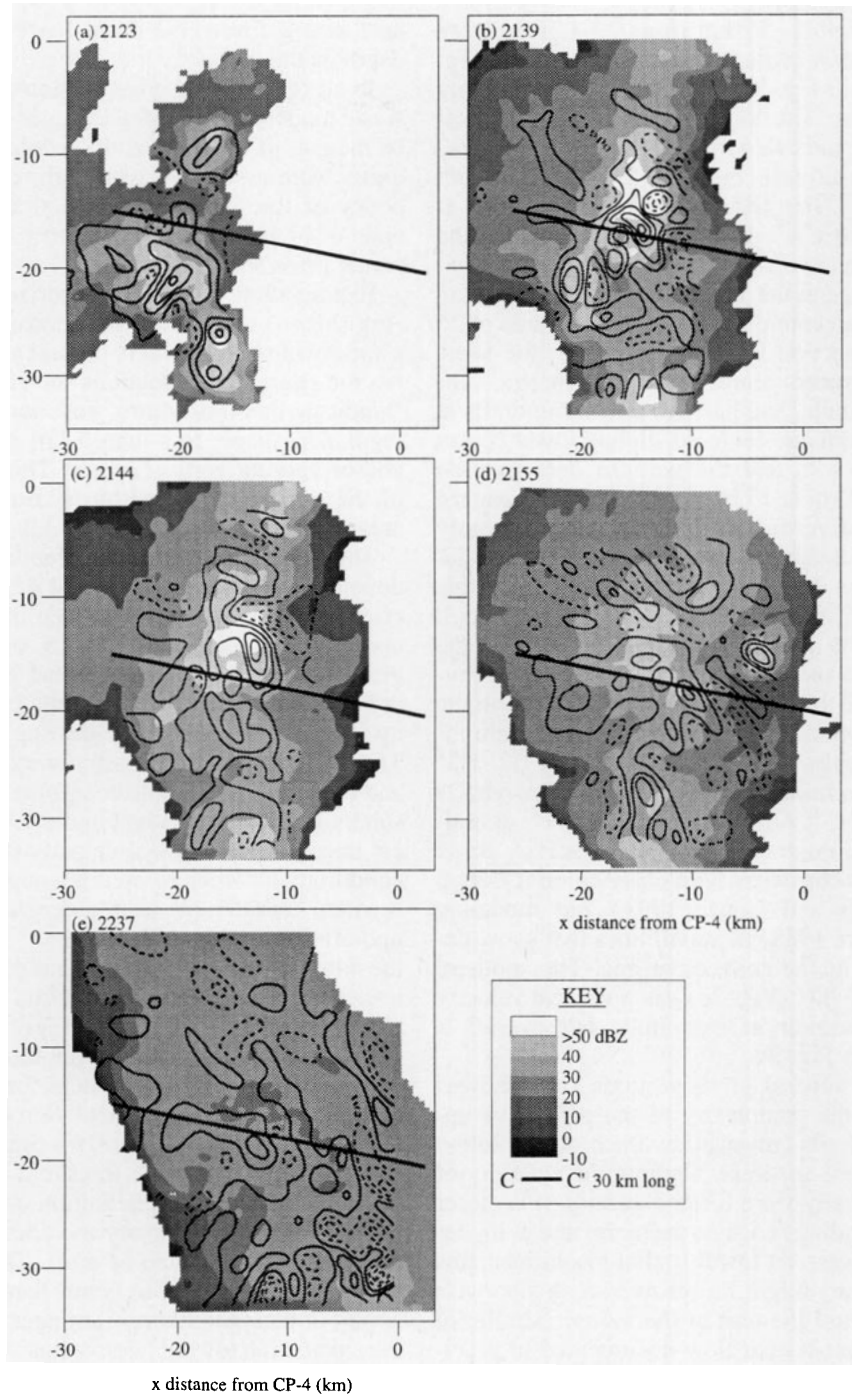
FIG. 8. Time series of horizontal cross sections of radar reflectivity and vertical velocity at the 8-km altitude. Heavy line C–C' indicates location of vertical cross sections in Fig. 9. Radar reflectivity is shaded at 10-dB intervals starting at −10 dBZ. The missing region in the reflectivity field in the northeast corner of the domain is an artifact of the dual Doppler scanning: (a) 2123 UTC, with contours of vertical velocity at −3, 3, 9, and 15 m s$^{-1}$, with negative values dashed; (b) 2139 UTC, with contours of vertical velocity at −9, −3, 3, 9, 15, 21, and 27 m s$^{-1}$, with negative values dashed; (c) 2144 UTC, with contours of vertical velocity at −15, −9, −3, 3, 9, 15, and 21 m s$^{-1}$, with negative values dashed; (d) 2155 UTC, with contours of vertical velocity at −9, −3, 3, 9, and 15 m s$^{-1}$, with negative values dashed; (e) 2237 UTC, with contours of vertical velocity at −5, −3, −1, 1, and 3 m s$^{-1}$, with negative values dashed.

= −14.5 km and $y = −17$ km from CP-4. Two more southwest–northeast cross sections (B2–B2′ in Fig. 7d and B3–B3′ in Fig. 7e) show the variation along the line of storms. The locations of all four vertical cross sections are indicated in the horizontal cross section at the 3.2-km altitude (Fig. 7a). In the north–south cross section (Fig. 7b), the strong updraft centered at $x = −14.5$ km and $y = −17$ km is tilted slightly to the north aloft and has two areas of maximum vertical velocity, one centered at the 7-km altitude at greater than 30 m s$^{−1}$ and one centered at the 11-km altitude at 25 m s$^{−1}$. In cross section B1–B1′ (Fig. 7c), the same strong updraft appears more or less symmetric, centered at 7-km altitude, and has two smaller updrafts at its sides, the eastern one centered slightly lower (5-km altitude at 20 m s$^{−1}$) and the western one centered slightly higher (9 km at 15 m s$^{−1}$). The overall pattern of reflectivity and vertical velocity in Fig. 7c grossly resembles that of a vertical cross section perpendicular to the leading edge of a typical multicellular squall line (e.g., Figs. 4 and 5 of Smull and Houze 1987), though this cross section is not quite normal to the line. On the eastern side of the section, updrafts starting at low levels coincided with the leading edge of the storm. In the middle of the section, updrafts and downdrafts are interspersed. The cross section to the north at B2–B2′ (Fig. 7d) shows a mixture of updrafts and downdrafts from −5 to 15 m s$^{−1}$. A downdraft of 15 m s$^{−1}$ at midlevels is near the edge of the radar reflectivity echo. This downdraft is consistent with observations (Knupp 1987; Biggerstaff and Houze 1993) and modeling (Fovell and Ogura 1988) of squall lines that show descent just ahead of the convective line. The southern cross section B3–B3′ (Fig. 7e) has a vertical velocity pattern that is weaker in magnitude but overall is roughly similar to Fig. 7c.

As additional vertical cross sections (not shown) were examined, the complexity of the pattern of updrafts and downdrafts (revealed by the high-resolution data) became more apparent. Updrafts of a variety of magnitudes generally were located at midlevels closer to the eastern (leading) edge of the storm and at higher altitudes farther west. At lower spatial resolutions, this pattern (Figs. 7c,e) might be resolved as a slantwise upward flow toward the rear of the system, similar to the ascending front-to-rear flow documented in previous dual-Doppler analyses of squall lines (Smull and Houze 1987; Roux 1988; Houze et al. 1989; Biggerstaff and Houze 1991a, 1993).

Both low-level (e.g., at LLD in Figs. 7b–e) and upper-level downdrafts (e.g., at ULD in Figs. 7b,d,e) were present. The downdrafts centered at TD near the center of the cross section in Fig. 7c appear to have been an upper-level downdraft and a lower-level downdraft collocated horizontally and nearly connecting in the vertical. Biggerstaff and Houze (1993) suggested that the upper- and lower-level downdrafts form separately and if located one above the other may then con-

nect into a transverse draft that extends through the depth of the storm.

In all four vertical cross sections (Figs. 7b–e) there was a tendency for mid- and upper-level downdrafts to be in areas of low reflectivity, while lower-level downdrafts were associated with high reflectivity. The tendency of the lower-level downdrafts to occur in the zone of high reflectivity is further evident in the horizontal cross section in Fig. 7a.

Examination of additional horizontal cross sections (not shown) indicated that updrafts and downdrafts at a variety of strengths were present at all levels throughout the storm. Cross sections such as those in Figs. 7–9 indicate that most drafts were somewhat spatially irregular in shape, less than 5 km in horizontal extent and of varying vertical extent. This visual impression of the size was verified by measuring the horizontal area of individual drafts at the 3.2- and 8-km levels.

The calculation of the area of individual updrafts and downdrafts was done in several steps using horizontal cross sections. In the initial step in the calculation of updrafts, the contiguous areas of vertical velocity greater than 2 m s$^{−1}$ were found. Since the threshold defining the drafts is low, potentially several individual updrafts may be connected into one conglomerate area. These larger areas were often very irregularly shaped and contained holes. The conglomerate areas would be subdivided into individual updrafts associated with local maximum in vertical velocity under the following condition. In order to split a conglomerate area into separate updrafts, the peak magnitude of the candidate updrafts had to be at least 2 m s$^{−1}$ greater than that of the minimum value between candidate peaks in all connected directions. If this condition was met, the individual candidate updrafts were split from the conglomerate area along the area of minimum vertical velocity between drafts. Analogous steps for areas less than −2 m s$^{−1}$ were used in the calculation of downdraft areas. Individual downdrafts were, for the most part, well delineated by the −2 m s$^{−1}$ threshold and rarely occurred in conglomerates. This definition of a draft is based on changes in vertical velocity and does not assume a characteristic shape or size of draft. The strict conditions for splitting will tend to count flanking weaker drafts as part of their neighboring stronger drafts and thus bias the calculation toward larger areas. A 2 m s$^{−1}$ threshold is suited for identifying the spectrum of individual drafts occurring during the convective stages of the storm. For consistency, the same threshold was used for all five times examined even though a 2 m s$^{−1}$ threshold captures only the stronger portion of the spectrum of drafts occurring at 2237 UTC.

The number of drafts of different sizes at the 3.2- and 8-km altitudes for each of the five times are shown in Fig. 10. The dimensions of the updrafts (obtained by taking the square root of the measured area) were typically less than 5 km (4 km for downdrafts). Since the data were filtered to remove velocity features less
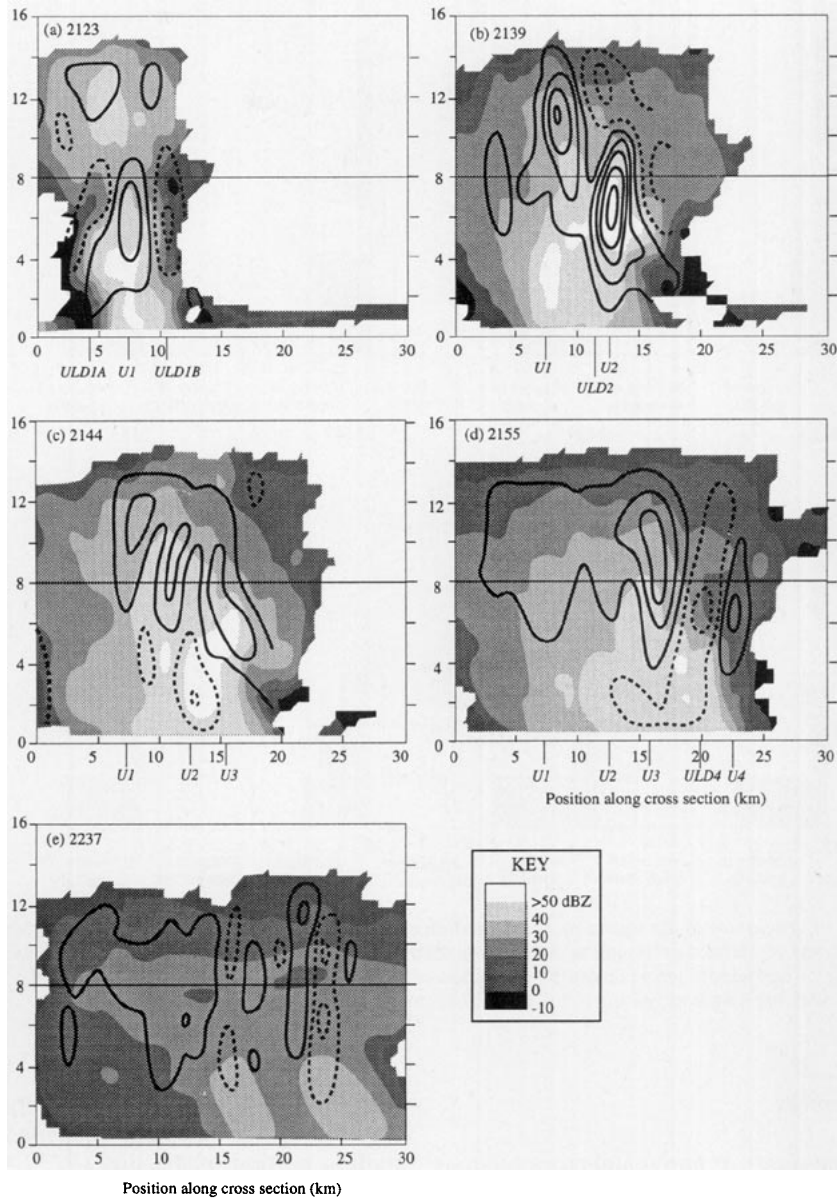
FIG. 9. Time series of vertical cross sections of radar reflectivity and vertical velocity along line C–C' (30 km long) indicated in Fig. 8. Radar reflectivity is shaded at 10-dB intervals starting at −10 dBZ. Height of the horizontal cross sections in Fig. 8 are indicated in the vertical cross sections by the horizontal line at 8 km. The horizontal position of the eastern-most (leading-edge) updraft at each time in the first four figures is indicated by U1, U2, U3, and U4. Horizontal positions of upper-level downdrafts in (a), (b), and (d) are designated by ULD suffix, where suffix is a unique identifier. (a) Contours of vertical velocity at −9, −3, 3; and 9 m s$^{-1}$, with negative values dashed. (b) Contours of vertical velocity at −9, −3, 3, 9, 15, 21, and 27 m s$^{-1}$, with negative values dashed. (c) Contours of vertical velocity at −9, −3, 3, and 9 m s$^{-1}$, with negative values dashed. (d) Contours of vertical velocity at −9, −3, 3, 9, and 15 m s$^{-1}$, with negative values dashed. (e) Contours of vertical velocity at −3, −1, 1, and 3 m s$^{-1}$, with negative values dashed.

than 2 km in horizontal extent (section 4), drafts smaller than a 2-km square-root area were below the resolvable resolution of this analysis and were not tab-

ulated. On average over the five times examined, 9 updrafts and 9 downdrafts were found at the 3.2-km level, and 11 updrafts and 7 downdrafts at the 8-km level.
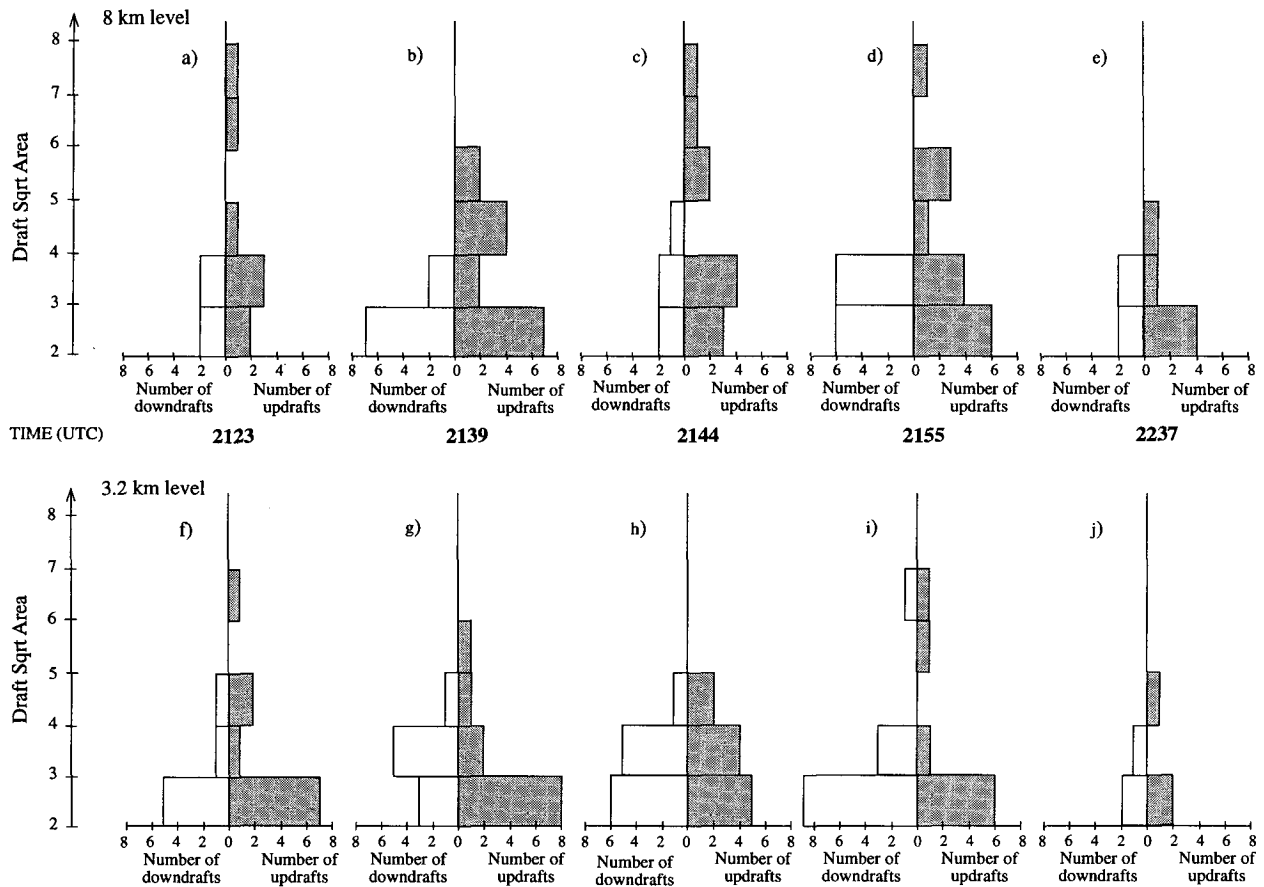
FIG. 10. Time series of histograms of the square root of downdraft and updraft areas at the 8- and 3.2-km altitudes. Histogram bin width is 2 m s$^{-1}$. Individual drafts are defined according to definition in text. Drafts of area less than or equal to 4 km$^2$ were not tabulated. Within each panel, the number of downdrafts are indicated by histogram with bar length increasing to the left, and the number of updrafts are indicated by histogram with bar length increasing to the right. The vertical axis is the square-root area of drafts.

## b. Temporal variability

Figure 8 is a time series of horizontal cross sections at 8 km. As the storm evolved from an early (2123 UTC, Fig. 8a) to vigorous stage (2139 UTC, Fig. 8b), the character of reflectivity at 8 km changed from a very cellular pattern with a close association of strong reflectivity and updrafts to a more contiguous reflectivity pattern as precipitation and, hence, reflectivity filled in between the updrafts. Upper-level downdrafts are present in these cross sections, and they appear to have been associated with the stronger updrafts. Downdrafts roughly encircled the updraft centered at $x = -14.5$ km, $y = -17$ km at 2139 in a manner somewhat analogous to chairs (downdrafts) surrounding a large table (strong updraft). In an idealized storm, with a single updraft, the surrounding upper-level downdrafts may be arranged more symmetrically (M. Weisman 1992, personal communication). As the storm matured (2144 UTC, Fig. 8c and 2155 UTC, Fig. 8d), the overall pattern of reflectivity weakened and began to lose its cel-

lular character, while individual drafts remained at the same horizontal scale but weakened in magnitude. The trailing portion of the line (2237 UTC, Fig. 8e) had nearly homogeneous reflectivity at 8 km and a pattern of very weak updrafts and downdrafts. The stronger updrafts and downdrafts tended to be located toward the east, closer to the leading edge of the storm.

The time resolution of the data is insufficient to follow a convective element unambiguously from one volume scan to the next. However, some insight can be gained by using the approximation that an updraft core at one time has indeed become the updraft element near that location at a subsequent time. This approximation is aided by the low vertical wind shear of the environment (Fig. 3b), in which isolated updraft parcels rise nearly vertically. Using the vertical cross sections (Fig. 9), we can coarsely follow the evolution of some updrafts. The roughly west-east line of the vertical cross sections in Fig. 9 is indicated by the line C-C' in the corresponding horizontal sections in Fig. 8. For the first four times, the position of the newest, most eastern up-

draft in the cross section is indicated on the horizontal axis. At subsequent times, the original position of the updraft is indicated to facilitate comparison with what is likely an updraft related to its original appearance. Each of the updraft elements seems to have drifted upward and eventually weakened. At 2123 UTC (Fig. 9a), an updraft of magnitude 10–15 m s$^{-1}$, centered at 4.5 km in height, was at horizontal location U1. This updraft likely became the upper-level updraft centered near 11 km and U1 at 2139 (Fig. 9b). It subsequently weakened in strength at 2144 (Fig. 9c) and 2155 (Fig. 9d). At 2139 (Fig. 9b), updraft U2 centered at 7 km in altitude had peak vertical velocities of 30–35 m s$^{-1}$. It weakened to 10–15 m s$^{-1}$ at 2155 (Fig. 9d) and moved upward to become centered at 11 km. Updraft U3, centered at 7 km in altitude at 2144 (Fig. 9c) drifted upward to 10 km and intensified by 2155 (Fig. 9d). Although these cross sections are in one vertical plane and the paths of the updrafts were not entirely within that plane, a trend of bubbles forming, rising, and weakening is indicated.

Lower-level downdrafts were located within the interior of the storm and associated spatially with higher reflectivities. Upper- and midlevel downdrafts were present in both lower- and higher-reflectivity areas. At 2123 UTC (Fig. 9a), two midlevel downdrafts at ULD1A and ULD1B surrounded the midlevel updraft at U1 and were centered near 5–6 km in altitude. Downdraft ULD1A was located near the western edge of the reflectivity echo and ULD1B near the eastern edge. Downdraft ULD1B was the stronger of the two and had a peak descent of −10 m s$^{-1}$. Both downdrafts had lower associated reflectivity than the updraft they bracketed at U1. At 2139 (Fig. 9b), an upper-level downdraft centered at ULD2 and 13-km altitude was at the same horizontal position as downdraft ULD1B in the 2123 volume. Downdraft ULD2 appears to have followed upward what was originally the updraft at U1 at 2123 UTC. At 2155 UTC (Fig. 9d), the level of peak descent for downdraft ULD4 was at the same level (7 km) as the peak ascent of updraft U4. A tendency for the mid- and upper-level downdrafts to be adjacent to the stronger mid- and upper-level updrafts is thus indicated.

At 2237 UTC (Fig. 9e), the vertical pattern of reflectivity is similar to that of a stratiform region of a squall line with broad areas of nearly horizontally homogenous reflectivity. However, a pattern of weak updrafts and downdrafts remains at 2237. To bring out the pattern of the drafts better, the vertical velocity contours in this figure were drawn at finer intervals (2 m s$^{-1}$) than in the cross sections for previous times. The updrafts and downdrafts appear to have been weakened remnants of drafts of the types seen earlier.

Flight-level data obtained by the SDSMT T-28 aircraft from 2126 to 2136 UTC (Figs. 11 and 12) during a roughly south–north pass through the higher-reflectivity areas of the storm provide a useful check on the
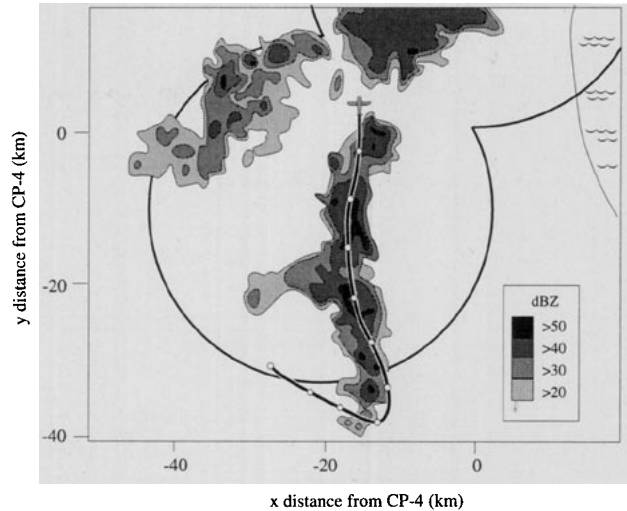


FIG. 11. Flight track of SDSMT T-28 aircraft along backbone of the storm in southern dual-Doppler lobe. The flight track from 2126 to 2136 UTC is superimposed on the CP-4 3° scan from 2136 UTC. White circles indicate plane's position at whole minutes; center of aircraft symbol at north end of track is position at 2136 UTC. Radar reflectivity is shaded at 10-dB intervals starting at 20 dBZ.

magnitudes of vertical velocity derived from the radar data. The flight altitude was between 5.4 and 5.7 km at temperatures of −4° to −9°C (Figs. 12a,b). A −15 m s$^{-1}$ downdraft was encountered at 2129 UTC (Fig. 12c). This midlevel downdraft was near cloud edge (indicated by the liquid water field in Fig. 12d) and adjacent to an updraft encountered just a few seconds earlier. The location and magnitude of this downdraft are consistent with the upper-level downdrafts seen in the radar data vertical cross sections (Figs. 8d and 9a). Just after 2131 UTC, a series of updrafts of varying magnitude and horizontal dimension was encountered by the aircraft. These included a strong narrow updraft with peak vertical velocity of 20 m s$^{-1}$ at 2131:30 UTC and an updraft maintaining ascent rates of greater than 10 m s$^{-1}$ for roughly 5.4-km along-track distance between 2133 and 2134 UTC. The horizontal configurations of these updrafts and their magnitudes are consistent with those seen in vertical cross sections of the radar data (Figs. 8b,c and 9a,b).

### c. Association between reflectivity and vertical velocity

Cross sections indicate the association between the fields they display at the points in space within the cross section. This association, for example, between the radar reflectivity and vertical velocity fields in Figs. 7–9, may or may not be typical of the entire echo volume. To examine these relationships in a statistical manner, scatter diagrams of reflectivity versus vertical velocity were plotted for two levels within the storm. These plots relate reflectivity and vertical velocity directly.
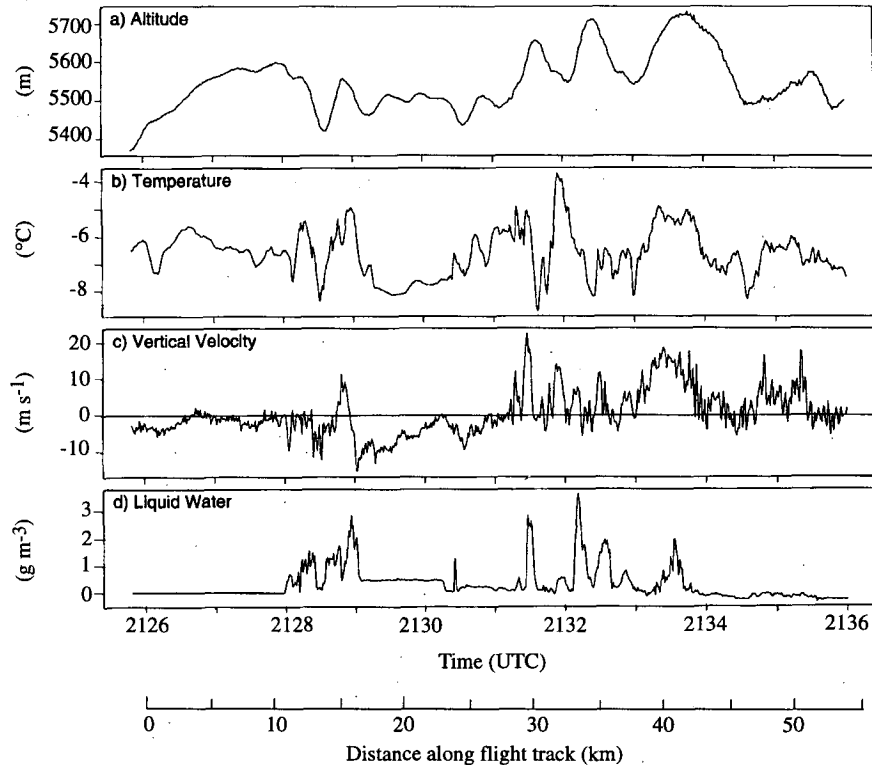
FIG. 12. Airborne SDSMT T-28 flight-level data (1-s intervals) along flight track shown in Fig. 11. The aircraft traveled at 90 m s$^{-1}$ (~5.4 km min$^{-1}$): (a) altitude; (b) temperature; (c) vertical velocity computed using method of Kopp (1985); and (d) liquid water (from Johnson–Williams probe).

Selected scatter diagrams are shown in Fig. 13. To simplify the reading of these plots, the density of points was contoured. These plots are not normalized. The scatter diagrams in Fig. 13 show results for one lower level (3.2 km) and one upper level (8 km) at an early (2139 UTC) and late (2237 UTC) stage of storm development. In general, the correlation between reflectivity and vertical velocity is weak. At best, particular ranges of reflectivity values tend to be associated with particular ranges of vertical velocity values. The weak statistical association is a caution on how generally the relationship between reflectivities and vertical velocities seen in the cross sections (Figs. 7–9) can be applied.

At 3.2 km within the 2139 UTC volume, higher reflectivities (>35 dBZ) tend to be associated with both updrafts and downdrafts (Fig. 13a). Thus, it cannot be said that at low levels heavy rain is exclusively contained within downdrafts. Moreover, both weak updrafts and weak downdrafts are associated with a wide range of reflectivity values at 2139 and 2237 UTC (Figs. 13a,c).

The scatterplot for 8.8 km at 2139 UTC (Fig. 13b) suggests that within the wide distribution of reflectivity values at this level in the early stages of the storm, lower reflectivities were associated with downdrafts. In particular, reflectivity values centered near 18 dBZ were associated with downdrafts of approximately −1 to −3 m s$^{-1}$. Higher reflectivities tended to occur as the vertical velocity increased. However, the association was somewhat diffuse (Fig. 13b). Although higher reflectivities tended to be in the stronger updrafts, these reflectivity values were also found within downdrafts (Fig. 13b). Later in the storm's development, both updrafts and downdrafts were associated with the narrow range of reflectivity values (Fig. 13d).

The diffuseness of the correlation between reflectivity and vertical velocity is an indicator of the mishmash of particle types, sizes, and concentrations contained in both updrafts and downdrafts within the storm. A potential explanation for the further weakening of the association between reflectivity and vertical velocity as the storm matured is that at later stages the heavier particles have fallen out and particles left by previous updrafts within the storm volume could have become collocated with subsequent downdrafts and updrafts.

## 6. Discussion

To learn something new about precipitation processes, we need to take full advantage of the high-spatial-resolution data the radars have provided. Cross sec-
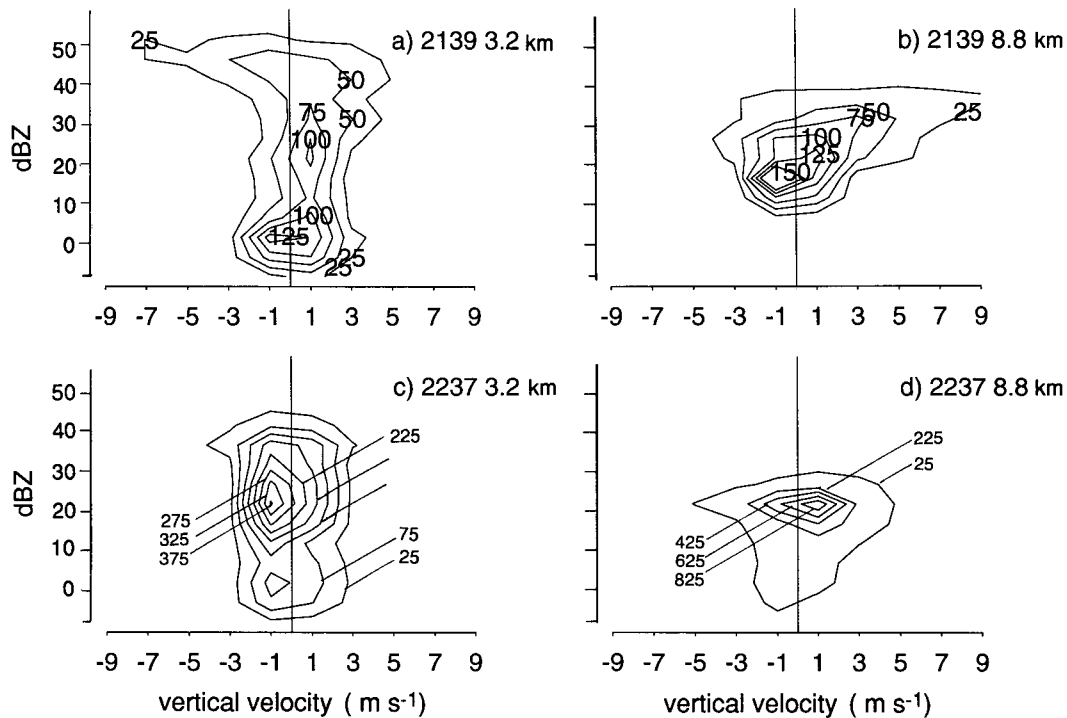
FIG. 13. Scatterplots of radar reflectivity versus vertical velocity. The number of points in bins of 5 dBZ and 1 m s$^{-1}$ are contoured: (a) 2139 UTC at the 3.2-km altitude, contoured starting at 25 points with contour interval of 25 points; (b) 2139 UTC at the 8.8-km altitude, contoured starting at 25 points with contour interval of 25 points; (c) 2237 UTC at 3.2 km, contoured starting at 25 points with contour interval of 50 points; (d) 2237 UTC at 8.8 km, contoured starting at 25 points with contour interval of 200 points.

tions of the high-resolution data reveal the complex small-scale variability of updrafts, downdrafts, and precipitation. However, it is evident from the cross sections just viewed that an attempt to characterize this storm completely by conventional cross sections would yield an unwieldy number of figures, and even a larger number of cross sections than included here would only partially show the storm structure.

Additionally, there is an inherent problem in taking a two-dimensional cross section through a set of variously shaped three-dimensional objects such as drafts in a multicellular storm. A vertical cut through the center of any one object in the set may cut through the center, graze the edge, or miss other objects completely. A graze along the edge of an updraft will make it appear weaker than if the updraft had been cut through its strongest point. The strongest magnitude within an updraft may not be in the geometric center of the draft. Thus, it is difficult, if not impossible, to make a representative two-dimensional cross section through a multicellular storm. It is also not clear from selected cross sections alone whether the characteristics observed are representative of the behavior of the entire storm. Indeed, the association between the reflectivity and the vertical velocity fields is statistically weaker than the cross sections imply. The evidence contained

in these cross sections is inherently anecdotal. The information they contain is useful only as a piece in the larger puzzle of what is occurring in the storm, and only as long as it is taken in context.

Thus, while some interpretation of the kinematic and microphysical structures for small areas can be made using cross sections such as these, the three-dimensional and highly variable structure of the storm as a whole does not lend itself readily to comprehension when represented by traditional horizontal and vertical cross sections. A method is needed that will overcome the limitations of cross sections, identify the salient ensemble properties of the storm, and reveal how these properties change as the storm evolves. A statistical methodology that accomplishes these goals will be introduced and exploited in YH Parts II and III.

## 7. Conclusions

This first part in a three-part study of the evolution of Florida cumulonimbus has laid the groundwork for the two subsequent papers by examining the storm setting and the spatial distribution of vertical velocity and precipitation. The centerpiece of this study is high-resolution dual-Doppler radar data collected during CaPE. The high-resolution radar data are a rich source of in-

formation on how the convective-to-stratiform transition of the storm occurred. Previous studies (Biggerstaff and Houze 1991a, 1993; Mapes and Houze 1993) have documented the convective and stratiform stages of the storm, but their lower-resolution radar data contained insufficient information to ascertain clearly the method of storm evolution.

The storm under study is an example of ordinary, typical sea-breeze convection with weak vertical wind shear. High-resolution dual-Doppler radar data documented the evolution of a line of storms that developed near the east coast of Florida and moved eastward.

This storm exhibited many of the typical line-normal characteristics of multicellular squall lines documented at lower resolutions. For example, updraft peak magnitudes were found at successively higher altitudes at increasing distance from the leading edge of the storm. This study provides new insights into the structure and evolution of the multicellular squall lines because of the high resolution of the data, and thus gives the opportunity to examine the detailed structure of the line in three dimensions. The line of storms was revealed by cross sections to have considerable along-line variation both spatially and temporally (Figs. 7–9). In detail, the storm was very three-dimensional. The high-resolution radar data revealed a complex jumble of updrafts, downdrafts, and precipitation. Although, by definition, horizontal and vertical cross sections are not necessarily representative of a complex three-dimensional structure, examination of cross sections suggests several trends in the structure and evolution of the storm that will be examined further in the subsequent papers.

- As the storm evolved, the radar reflectivity became more contiguous as radar echo filled in between individual cells at upper levels.
- Most of the radar echo volume of the storm contained irregularly shaped drafts less than 5 km in horizontal extent and of varying vertical extent.
- At any given time, updrafts and downdrafts at a variety of strengths were present at all levels throughout the storm.
- The stronger updrafts tended to be located closer to the leading edge of the storm.
- Upper-level downdrafts tended to be located at the sides of the stronger upper-level updrafts.
- The evolution of updrafts indicated a tendency to behave in a bubble-like fashion: forming at low levels, rising within the echo volume, and eventually weakening at upper levels.
- The updrafts and downdrafts present in the later periods of the storm appear to be the weakened remnants of drafts of the types seen earlier.
- Scatterplots of reflectivity versus vertical velocity reveal only a weak association between reflectivity values and updraft and downdraft magnitudes that become more diffuse as the storm ages.

The high-resolution data have suggested these conclusions. However, traditional case study analysis, based on horizontal and vertical cross sections, leaves us only with impressions that are not rigorously shown. It is evident from this first phase of the study that new analysis methods are needed to take full advantage of the high-resolution radar data. In YH Part II and YH Part III, the impressions gained from cross sections will be tested quantitatively and put in context using a method for statistically characterizing the entire volume of the radar data.

## REFERENCES

Battan, L. J., 1973: *Radar Observation of the Atmosphere.* University of Chicago Press, 324 pp.

Biggerstaff, M. I., and R. A. Houze Jr., 1991a: Kinematic and precipitation structure of the 10–11 June 1985 squall line. *Mon. Wea. Rev.,* **119,** 3035–3065.

——, and ——, 1991b: Midlevel vorticity structure of the 10–11 June 1985 squall line. *Mon. Wea. Rev.,* **119,** 3066–3079.

——, and ——, 1993: Kinematics and microphysics of the transition zone of a midlatitude squall-line system. *J. Atmos. Sci.,* **50,** 3091–3110.

Blanchard, D. O., and R. E. Lopez, 1985: Spatial patterns of convection in south Florida. *Mon. Wea. Rev.,* **113,** 1282–1299.

Braun, S. A., and R. A. Houze Jr., 1994: The transition zone and secondary maximum of radar reflectivity behind a midlatitude squall line: Results retrieved from Doppler radar data. *J. Atmos. Sci.,* **51,** 2733–2755.

Brock, F. V., and P. K. Govind, 1977: Portable automated mesonet in operation. *J. Appl. Meteor.,* **16,** 299–310.

——, and G. H. Saum, 1983: Portable Automated Mesonet II. Preprints, *Fifth Symp. of Meteorological Observations and Instrumentation,* Toronto, Canada, Amer. Meteor. Soc., 314–320.

Burghart, C., P. J. Wyngaard, P. H. Herzegh, and J. W. Wilson, 1989: A program for optimization of meteorological radar scanning. Preprints, *24th Conf. on Radar Meteorology,* Tallahassee, FL, Amer. Meteor. Soc., 573–576.

Burpee, R. W., and L. N. Lahiff, 1984: Area-average rainfall variations on sea-breeze days in south Florida. *Mon. Wea. Rev.,* **112,** 520–534.

Byers, H. R., and R. R. Braham, Jr., 1949: *The Thunderstorm.* U.S. Government Printing Office, 287 pp.

Churchill, D. D., and R. A. Houze, Jr., 1984: Development and structure of winter monsoon cloud clusters on 10 December 1978. *J. Atmos. Sci.,* **41,** 933–960.

Cunning, J. B., 1986: The Oklahoma–Kansas Preliminary Regional Experiment for STORM-Central. *Bull. Amer. Meteor. Soc.,* **67,** 1478–1486.

Davies-Jones, R. P., 1979: Dual-Doppler radar coverage area as a function of measurement accuracy and spatial resolution. *J. Appl. Meteor.,* **18,** 1229–1233.

Detweiler, A. G., and P. L. Smith, 1992: T-28 participation in the Convection and Precipitation/Electrification (CaPE) Experiment. Report SDSMT/IAS/R-92/04, Institute of Atmospheric Sciences, South Dakota School of Mines and Technology, Rapid City, SD, 76 pp.

Fovell, R. G., and Y. Ogura, 1988: Numerical simulation of a midlatitude squall line in two dimensions. *J. Atmos. Sci.,* **45,** 3846–3879.

Galway, J. G., 1956: The lifted index as a predictor of latent instability. *Bull. Amer. Meteor. Soc.,* **37,** 528–529.

Gentry, R. C., and P. L. Moore, 1954: Relation of local and general wind interaction near the sea coast to time and location of airmass showers. *J. Meteor.,* **11,** 507–511.

Heymsfield, G. M., and S. Schotz, 1985: Structure and evolution of a severe squall line over Oklahoma. *Mon. Wea. Rev.,* **113,** 1563–1589.

Houghton, H. G., 1968: On precipitation mechanisms and their artificial modification. *J. Appl. Meteor.,* **7,** 851–859.

Houze, R. A., Jr., 1973: A climatological study of vertical transports by cumulus-scale convection. *J. Atmos. Sci.,* **30,** 1112–1223.

——, 1981: Structures of atmospheric precipitation systems: A global survey. *Radio Sci.,* **16,** 671–689.

——, 1989: Observed structure of mesoscale convective systems and implications for large-scale heating. *Quart. J. Roy. Meteor. Soc.,* **115,** 425–461.

——, 1993: *Cloud Dynamics.* Academic Press, 573 pp.

——, S. A. Rutledge, M. I. Biggerstaff, and B. F. Smull, 1989: Interpretation of Doppler weather-radar displays in midlatitude mesoscale convective systems. *Bull. Amer. Meteor. Soc.,* **70,** 608–619.

——, B. F. Smull, and P. Dodge, 1990: Mesoscale organization of springtime rainstorms in Oklahoma. *Mon. Wea. Rev.,* **117,** 613–654.

Huschke, R. E., Ed., 1959: *Glossary of Meteorology.* American Meteorological Society, 638 pp.

Johnson, G. N., and P. L. Smith Jr., 1980: Meteorological instrumentation system on the T-28 thunderstorm research aircraft. *Bull. Amer. Meteor. Soc.,* **61,** 972–979.

Kessinger, C. J., P. S. Ray, and C. E. Hane, 1987: The 19 May 1977 Oklahoma squall line. Part I: A multiple Doppler analysis of convective and stratiform structure. *J. Atmos. Sci.,* **44,** 2840–2864.

——, D. B. Parsons, and J. W. Wilson, 1988: Observations of a storm containing mesocyclones, downbursts, and horizontal vortex circulations. *Mon. Wea. Rev.,* **116,** 1959–1982.

Kingsmill, D. E., and R. M. Wakimoto, 1991: Kinematic, dynamic, and thermodynamic analysis of a weakly sheared severe thunderstorm over northern Alabama. *Mon. Wea. Rev.,* **119,** 262–297.

Knupp, K. R., 1987: Downdrafts within High Plains cumulonimbi. Part I: General kinematic structure. *J. Atmos. Sci.,* **44,** 987–1008.

——, 1988: Downdrafts within High Plains cumulonimbi. Part II: Dynamics and thermodynamics. *J. Atmos. Sci.,* **45,** 3965–3982.

Kopp, F. J., 1985: Deduction of vertical motion in the atmosphere from aircraft measurements. *J. Atmos. Oceanic Technol.,* **2,** 684–688.

Lauritsen, P., Z. Mulekmadanic, C. Movel, and R. McBeth, 1987: The cross-chain LORAN atmospheric sounding system (CLASS). Preprints, *Sixth Symp. on Meteorological Observations and Instrumentation,* New Orleans, LA, Amer. Meteor. Soc., 340–343.

Leary, C. A., 1984: Precipitation structure of the cloud clusters in a tropical easterly wave. *Mon. Wea. Rev.,* **112,** 313–325.

——, and R. A. Houze Jr., 1979: Melting and evaporation of hydrometeors in precipitation from the anvil clouds of deep tropical convection. *J. Atmos. Sci.,* **36,** 669–679.

Leise, J. A., 1981: A multi-dimensional scale-telescoped filter and data extension package. NOAA Tech. Memo, WPL-82, 20 pp.

Mapes, B. E., and R. A. Houze Jr., 1992: An integrated view of the 1987 Australian monsoon and its mesoscale convective systems. Part I: Horizontal structure. *Quart. J. Roy. Meteor. Soc.,* **118,** 927–963.

——, and ——, 1993: An integrated view of the 1987 Australian monsoon and its mesoscale convective systems. Part II: Vertical structure. *Quart. J. Roy. Meteor. Soc.,* **119,** 733–754.

Marks, F. D., Jr., and R. A. Houze Jr., 1987: Inner-core structure of Hurricane Alicia from airborne Doppler-radar observations. *J. Atmos. Sci.,* **44,** 1296–1317.

Matejka, T. J., and R. C. Srivastava, 1991: An improved version of the extended velocity-azimuth display analysis of single-Doppler radar data. *J. Atmos. Oceanic Technol.,* **8,** 453–466.

Mohr, C. G., and R. L. Vaughn, 1979: An economical procedure for Cartesian interpolation and display of reflectivity factor in three-dimensional space. *J. Appl. Meteor.,* **18,** 661–670.

——, and L. J. Miller, 1983: CEDRIC — A software package for Cartesian space editing, synthesis and display of radar fields under interactive control. Preprints, *21st Conf. on Radar Meteorology,* Edmonton, Canada, Amer. Meteor. Soc., 559–574.

Nicholls, M. E., R. A. Pielke, and W. R. Cotton, 1991: A two-dimensional numerical investigation of the interaction between sea breezes and deep convection over the Florida peninsula. *Mon. Wea. Rev.,* **119,** 298–323.

O'Brien, J. E., 1970: Alternative solutions to the classical vertical velocity problem. *J. Appl. Meteor.,* **9,** 197–203.

Oye, R., and R. E. Carbone, 1981: Interactive Doppler editing software. Preprints, *20th Conf. on Radar Meteorology,* Boston, MA, Amer. Meteor. Soc., 683–689.

Ray, P. S., and K. L. Sangren, 1983: Multiple-Doppler radar network design. *J. Climate Appl. Meteor.,* **22,** 1444–1454.

——, C. L. Ziegler, W. Bumgarner, and R. J. Serafin, 1980: Single- and multiple-Doppler radar observations of tornadic storms. *Mon. Wea. Rev.,* **108,** 1607–1625.

Raymond, D. J., R. Solomon, and A. M. Blyth, 1991: Mass fluxes in New Mexico mountain thunderstorms from radar and aircraft measurements. *Quart. J. Roy. Meteor. Soc.,* **117,** 587–621.

Rinehart, R. E., 1991: *Radar for Meteorologists,* 2d ed. Department of Atmospheric Sciences, University of North Dakota, 334 pages.

Roux, F., 1988: The west African squall line observed on 23 June 1981 during COPT 81: Kinematics and thermodynamics of the convective region. *J. Atmos. Sci.,* **45,** 406–426.

Smull, B. F., and R. A. Houze Jr., 1987: Dual-Doppler radar analysis of a midlatitude squall line with a trailing region of stratiform rain. *J. Atmos. Sci.,* **44,** 2128–2148.

——, and J. A. Augustine, 1993: Multiscale analysis of a mature mesoscale convective complex. *Mon. Wea. Rev.,* **121,** 103–132.

Srivastava, R. C., 1985: A simple model of evaporatively driven downdraft application to microburst downdraft. *J. Atmos. Sci.,* **42,** 1004–1023.

——, 1987: A model of intense downdrafts driven by the melting and evaporation of precipitation. *J. Atmos. Sci.,* **44,** 1752–1773.

Steiner, M., 1991: A new relationship between mean Doppler velocity and differential reflectivity. *J. Atmos. Oceanic Technol.,* **8,** 430–443.

Webster, P. J., and R. A. Houze Jr., 1991: The Equatorial Mesoscale Experiment (EMEX): An overview. *Bull. Amer. Meteor. Soc.,* **72,** 1481–1505.

Weisman, M. L., and J. B. Klemp, 1982: The dependence of numerically simulated convective storms on vertical wind shear and buoyancy. *Mon. Wea. Rev.,* **110,** 504–520.

Wilson, J. W., and D. Reum, 1988: The flare echo: Reflectivity and velocity signature. *J. Atmos. Oceanic Technol.,* **5,** 197–205.

——, R. D. Roberts, C. Kessinger, and J. McCarthy, 1984: Microburst wind structure and evaluation of Doppler radar for airport wind shear detection. *J. Climate Appl. Meteor.,* **23,** 898–915.

——, T. M. Weckwerth, J. Vivekanandan, R. M. Wakimoto, and R. W. Russell, 1994: Boundary layer clear-air radar echoes: Origin of echoes and accuracy of derived winds. *J. Atmos. Oceanic Technol.,* **11,** 1184–1206.

Yuter, S. E., and R. A. Houze Jr., 1995a: Three-dimensional kinematic and microphysical evolution of Florida cumulonimbus. Part II: Frequency distributions of vertical velocity, reflectivity, and differential reflectivity. *Mon. Wea. Rev.,* **123,** 1941–1963.

——, and ——, 1995b: Three-dimensional kinematic and microphysical evolution of Florida cumulonimbus. Part III: Vertical mass transport, mass divergence, and synthesis. *Mon. Wea. Rev.,* **123,** 1964–1983.